Materials Research. 2020; 23(1): e20190627
DOI: https://doi.org/10.1590/1980-5373-MR-2019-0627

Physical and Photocatalytic Properties of $CeO_2/ZnO/ZnAl_2O_4$ Ternary Nanocomposite Prepared by Co-precipitation Method

Wararat Somraksa[a], Sumetha Suwanboon[a], Pongsaton Amornpitoksuk[b], Chamnan Randorn[c,d]*

[a]*Prince of Songkla University, Faculty of Science, Department of Materials Science and Technology, Hat Yai, Songkhla 90110, Thailand*
[b]*Prince of Songkla University, Faculty of Science, Department of Chemistry and Center of Excellence for Innovation in Chemistry, Hat Yai, Songkhla 90110, Thailand*
[c]*Chiang Mai University, Faculty of Science, Department of Chemistry, Chiang Mai 50200, Thailand*
[d]*Chiang Mai University, Faculty of Science, Materials Science Research Center, Chiang Mai 50200, Thailand*

Received: November 11, 2019; Revised: January 20, 2020; Accepted: January 24, 2020

$ZnAl_2O_4$ spinel nanoparticles and $CeO_2/ZnO/ZnAl_2O_4$ ternary nanocomposites were synthesized by a co-precipitation method. The structural, morphological, optical properties and chemical compositions of the products were analyzed respectively by X-ray diffraction (XRD), scanning electron microscopy (SEM), diffuse reflectance spectroscopy (DRS) and X-ray fluorescence (XRF) spectroscopy. The optical band gap of $ZnAl_2O_4$ spinel nanoparticles was 3.220 eV. When 1.0 mmol $Ce(NO_3)_3 \cdot 6H_2O$ was added to the synthesis reaction, the optical band gap of the obtained ternary nanocomposite was 3.170 eV. The influence of phase composition, optical band gap, oxygen vacancy and specific surface area on photocatalytic activity over $CeO_2/ZnO/ZnAl_2O_4$ ternary nanocomposites was investigated. The $CeO_2/ZnO/ZnAl_2O_4$ nanocomposite prepared with 1.0 mmol $Ce(NO_3)_3 \cdot 6H_2O$ showed the lowest recombination rate of photoexcited electron-hole pairs, the narrowest optical band gap (3.170 eV) and the highest oxygen vacancy concentration or highest Urbatch energy (0.299 eV). These parameters produced the best photocatalytic activity toward methylene blue (MB) under UV irradiation. The $CeO_2/ZnO/ZnAl_2O_4$ ternary nanocomposites exhibited better photocatalytic performance than pure $ZnAl_2O_4$ spinel nanoparticles and 100% degradation of aqueous MB solution was achieved within 60 min when using the $CeO_2/ZnO/ZnAl_2O_4$ ternary nanocomposite photocatalyst synthesized with 1.0 mmol $Ce(NO_3)_3 \cdot 6H_2O$.

Keywords: *nanocomposite; chemical synthesis; optical properties; photocatalytic properties.*

1. Introduction

In recent years, the paper, textile, leather and cosmetic industries have developed rapidly worldwide. These industries attract customers by coloring their products with a range of synthetic organic dyes. When the use of synthetic organic dyes increases, the amount of wastewater produced also increases. To reduce pollution, factories must remove synthetic organic dyes in wastewater before they are discharged into natural waterways. The elimination of synthetic organic dyes from wastewater is accomplished by biological, coalescence and adsorption methods[1]. However, since these methods cannot completely get rid of the synthetic organic dyes in a single step, further treatment is necessary. The photocatalytic process is another popular method of eliminating dyes. Removing the remaining dye in wastewater by photocatalytic degradation has several advantages; for example, photocatalytic conditions are mild, the use of chemical reagents is reduced, and synthetic organic dyes can be degraded to small non-toxic molecules[2,3]. In photocatalytic degradation, the photocatalyst used is very important to the process. Therefore, the choice of photocatalyst is the primary consideration and a summary of the many different photocatalysts that have been used is presented in Table 1.

Recently, AB_2O_4 spinel oxides, in which A is a divalent metal ion and B is a trivalent metal ion, have gained attention from many research groups[4,26-31]. This interest has led to their applications in water splitting, gas sensing, transparent conducting materials and photocatalysis. Zinc aluminate ($ZnAl_2O_4$), a spinel oxide with a wide band gap of about 3.8 eV, is an important member of the AB_2O_4 spinel oxides. Applications of $ZnAl_2O_4$ include dosimetry[32], opto-electronic devices[33], gas sensing[34], ceramic support[35] and photocatalysis[5]. The unique properties of $ZnAl_2O_4$ spinel nanoparticles depend on various parameters and researchers have improved these properties by doping with divalent[36-38] or trivalent[39-41] metal ions, and loading with secondary metal oxide powders[6,41]. $ZnAl_2O_4$ spinel nanoparticles have been synthesized by vibrational ball milling[42], hydrothermal synthesis[43], sol-gel synthesis[39], combustion[41] and co-precipitation[44]. The advantages of the co-precipitation method include low temperature preparation, high purity products, simple procedure and easy scalability[7,8].

The present work proposes a co-precipitation synthesis of $CeO_2/ZnO/ZnAl_2O_4$ ternary nanocomposites using KOH solution as the precipitating agent. This process has not, to our knowledge, been reported previously. The synthesized nanocomposites were used in the photocatalytic degradation of MB. The chosen dye model enabled the assessment of the

*e-mail: ssuwanboon@yahoo.com; sumetha.s@psu.ac.th.

Table 1. Summary of photocatalysts used in dye degradation processes.

Researcher	Catalyst	Dye	Light source	Irradiation time (min)	%Degradation
Suwanboon et al.[2]	ZnO	MB	UV black light (18 W)	180	100
		MB	Visible light	180	98
Akika et al.[4]	$Ni_{0.2}Cu_{0.8}Al_2O_4$	Congo red (CR)	Solar light (750 W/m^2)	180	90.6
Chaudhary[5]	$ZnAl_2O_4$	CR	Mercury lamp (500 W)	80	97.2
		Methyl orange (MO)	Mercury lamp (500 W)	80	96.9
		MB	Mercury lamp (500 W)	80	90.2
Zhang et al.[6]	25%ZnO/$ZnAl_2O_4$	MO	Xenon lamp (150 W)	60	98.7
Sumathi et al.[7]	$ZnAl_{1.98}Ce_{0.02}O_4$	MB	UV light (32 W)	25	99.3
			Tungsten lamp (500 W)	240	45.6
Suwanboon et al.[8]	ZnO	MB	UV black light (15 W)	90	100
Suwanboon et al.[9]	$Zn_{0.95}La_{0.05}O$	MB	UV black light (18 W)	150	98
	$Zn_{0.95}Mg_{0.05}O$	MB	UV black light (18 W)	120	100
Khan et al.[10]	p-CeO_2	MB	Tungsten lamp (400 W)	360	30
Klubnuan et al.[11]	ZnO	MB	UV black light (18 W)	75	100
Lv et al.[12]	1%CeO_2/ZnO	MB	Mercury lamp (500 W)	110	100
Zhang et al.[13]	ZnO/NiO/$ZnAl_2O_4$	MO	Xenon lamp (150 W)	60	97.3
Balamurugan et al.[14]	CdO/Al_2O_3	Metanil yellow (MY)	Visible light	75	82.1
Chen et al.[15]	ZnO/Zn foil	MO	Mercury lamp (300 W)	240	100
Kirankumar et al.[16]	$ZnAl_{1.99}Bi_{0.01}O_4$	MB	Xenon lamp (250 W)	240	100
Saleh et al.[17]	MWCNT/TiO_2	MO	UV lamp (40 W)	100	93
Saravanan et al.[18]	PANI/ZnO	MO	Projection lamp (250 W)	180	98.3
		MB	Projection lamp (250 W)	180	99.2
Saravanan et al.[19]	95%ZnO/5%CuO	MO	Projection lamp (250 W)	120	97.2
		MB	Projection lamp (250 W)	120	87.7
Saravanan et al.[20]	Hg:ZnO	MO	Projection lamp (250 W)	120	90
		MB	Projection lamp (250 W)	60	100
Saleh et al.[21]	MWCNT/WO_3	Rhodamine B (RhB)	Solar	150	100
Saravanan et al.[22]	ZnO/Ag/CdO	MB	Projection lamp (250 W)	90	98.3
Saravanan et al.[23]	ZnO/Ag/Mn_2O_3	Textile effluent	Visible light	180	98
Zhao et al.[24]	Au-Ag@$Bi_4Ti_3O_{12}$	RhB	Xenon lamp	120	95.5
		RhB	Mercury lamp	120	99.9
		RhB	Halogen-tungsten lamp	120	49.6
Yan et al.[25]	Bi@BiOCl	RhB	Xenon lamp	30	91.1

suitability of the photocatalyst for applications in several industries. Photocatalytic activity over the CeO_2/ZnO/$ZnAl_2O_4$ ternary nanocomposites was characterized to determine its dependence on structural, morphological and optical properties of the photocatalyst.

2. Experimental

2.1 Material

Zinc nitrate tetrahydrate ($Zn(NO_3)_2$•$4H_2O$, Emsure®, Germany), aluminium nitrate nonahydrate ($Al(NO_3)_3$•$9H_2O$, Sigma-Aldrich, Germany), cerium (III) nitrate hexahydrate ($Ce(NO_3)_3$•$6H_2O$, Aldrich, China), potassium hydroxide (KOH, Emsure®, Germany), and methylene blue ($C_{16}H_{18}ClN_3S$, Emsure®, Germany) were purchased and used without further purification.

2.2 Synthesis of $ZnAl_2O_4$ spinel nanoparticles

$ZnAl_2O_4$ spinel nanoparticles were synthesized by a co-precipitation method. Following stoichiometric calculations, 0.005 mol $Zn(NO_3)_2$•$4H_2O$ and 0.01 mol $Al(NO_3)_3$•$9H_2O$ were weighed and dissolved in 100 mL distilled water for 15 min under moderate stirring by a magnetic bar. Then, 0.04 mol KOH dissolved in 100 mL distilled water was added dropwise into the prepared mixture solution of Zn^{2+} and Al^{3+} ions. The white precipitates obtained were continuously stirred and heated at 70°C for 1 h. After the reaction was terminated

and cooled to room temperature, the precipitates were washed three times with 200 mL distilled water, filtered and dried at 80°C for 2 h. Finally, the as-synthesized powders were calcined in air at 800°C for 1 h and the calcined powders were later characterized by various techniques.

2.3 Synthesis of $CeO_2/ZnO/ZnAl_2O_4$ nanocomposites

To enable investigation of the effect of CeO_2 and ZnO loadings on the $ZnAl_2O_4$ nanocomposites, 0.2, 0.4, 0.6, 0.8 and 1.0 mmol $Ce(NO_3)_3•6H_2O$ were introduced separately into 100 mL mixture solutions prepared, as described in section 2.2, from 0.005 mol $Zn(NO_3)_2•4H_2O$ and 0.01 mol $Al(NO_3)_3•9H_2O$. The precursor solutions were then precipitated with 0.04 mol KOH dissolved in 100 mL distilled water. The synthesis then proceeded in the same way as the synthesis of pure $ZnAl_2O_4$ spinel nanoparticles.

2.4 Characterization

Thermal gravimetric analysis (TGA) was used to investigate the thermal behavior of as-synthesized $ZnAl_2O_4$ spinel nanoparticles. The TGA thermogram was recorded by thermogravimetric analyzer (TGA 7, Perkin Elmer) under nitrogen gas. X-ray diffraction (XRD) was used to analyze $ZnAl_2O_4$ spinel nanoparticles and secondary phases (CeO_2 and ZnO). XRD patterns were recorded by powder X-ray diffractometer (XRD, X′Pert MPD, Philips). X-ray fluorescence spectrometry (XRF, Zetium, PANalytical) was used to analyze the chemical composition of synthesized products. Scanning electron microscope (SEM) was used to observe the morphology of samples. The secondary electron images (SEI) were obtained by scanning electron microscope (SEM, Quanta 400, FEI). Brunauer-Emmett-Teller (BET) surface area analysis was used to determine the specific surface area (SA) of powders. The adsorption isotherm was measured by BET surface area analyzer (Autosorb 1MP, Quantachrome). Diffuse reflection spectroscopy (DRS) was used to study the optical behavior and evaluate the optical band gap of powders. Absorbance spectra were measured by UV-Vis spectrophotometer (UV-Vis 2450, Shimadzu). To evaluate remaining MB concentration, the absorbance of MB solutions was measured by UV-Vis spectroscopy and temporal changes were recorded by UV-Vis spectrophotometer (UV-Vis Lambda 25, Perkin Elmer).

2.5 Photocatalytic test

The photocatalytic activity of $ZnAl_2O_4$ spinel nanoparticles and $CeO_2/ZnO/ZnAl_2O_4$ ternary nanocomposites was evaluated by the degradation of aqueous MB solution under UV irradiation (3 parallel blacklight tubes, 15 W). In the typical procedure, 150 mg of photocatalyst were introduced into a 250 mL beaker containing 150 mL of 1×10^{-5} M MB solution. Before irradiation, the suspension was continuously stirred with a magnetic bar for 30 min in darkness to attain adsorption-desorption equilibrium between the MB and photocatalyst. The suspension was then irradiated and 3 mL of the suspension were withdrawn every 30 min and centrifuged at 4000 rpm for 5 min to separate the photocatalyst. The absorbance of the supernatant was recorded between 400 and 800 nm to determine the remaining MB and calculate the percentage of MB degradation.

3. Results and Discussion

3.1 Thermal analysis

In the experimental procedure, reagents were mixed in distilled water and reacted with each other to form a new compound. The thermal decomposition of representative as-synthesized powders was analyzed to determine an appropriate calcination temperature to obtain a pure $ZnAl_2O_4$ phase. The thermal analysis proceeded from room temperature to 1,000°C at a heating rate of 10°C/min under nitrogen gas.

Thermal decomposition comprised three steps (Figure 1). The first weight loss of about 9%, between room temperature and 180°C, was due to the removal of physically adsorbed molecular water[45]. The second weight loss of about 27%, between 180 and 500°C, derived from the elimination of structural water[8]. The third weight loss of about 3%, between 500 and 750°C, was attributed to the removal of nitrates[46]. No weight loss occurred above 750°C. Therefore, before characterization, the powders were calcined at 800°C in air for 1 h.

3.2 X-ray diffraction study

The phase formation of nanocomposites was identified from X-ray diffraction patterns of calcined samples (Figure 2). The diffraction peaks of cerium dioxide (CeO_2)

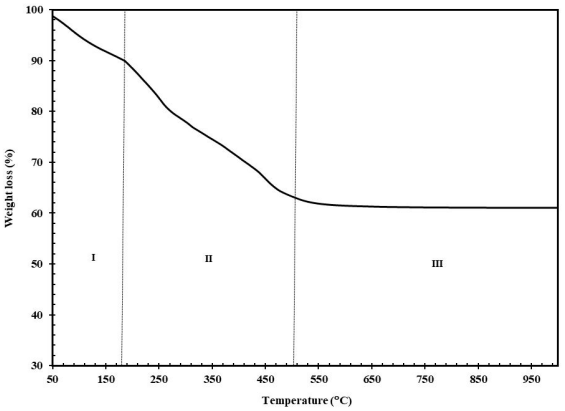

Figure 1. Thermal behavior of representative sample of as-synthesized $ZnAl_2O_4$ powder.

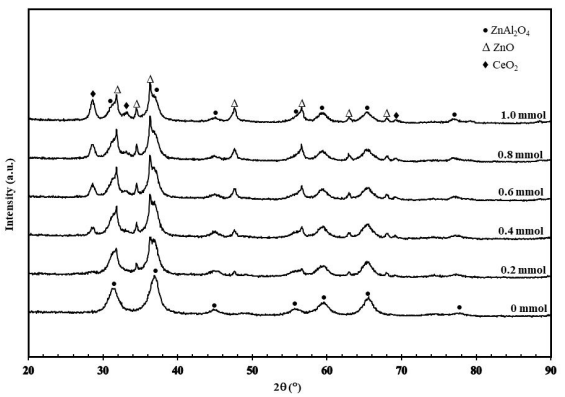

Figure 2. XRD patterns of $CeO_2/ZnO/ZnAl_2O_4$ nanocomposites prepared at different $Ce(NO_3)_3•6H_2O$ concentrations.

appeared at 2θ diffraction angles of 28.58°, 33.18° and 79.37° (JCPDS 34-0394). The diffraction peaks of zinc oxide (ZnO) appeared at 2θ diffraction angles of 31.80°, 34.47°, 36.30°, 47.58°, 56.59°, 62.95°, 67.95° and 69.36° (JCPDS 36-1451) and the diffraction peaks of zinc aluminate ($ZnAl_2O_4$) appeared at 2θ diffraction angles of 31.60°, 36.97°, 44.78°, 55.56°, 59.72° and 65.58° (JCPDS 05-0669). A pure $ZnAl_2O_4$ spinel phase formed without a ZnO secondary phase when $Ce(NO_3)_3$•$6H_2O$ was not present in the precursor solution. Therefore, the chemical reactions that occurred in this process can be expressed as reactions (1−3)[47]:

$$Zn(NO_3)_{2(aq)} + 2Al(NO_3)_{3(aq)} + 8KOH_{(aq)} \rightarrow Zn(OH)_{2(s)} + 2Al(OH)_{3(s)} + 8KNO_{3(aq)} \quad (1)$$

$$Zn(OH)_{2(s)} + 2Al(OH)_{3(s)} + 8KNO_{3(aq)} \xrightarrow{\Delta} (ZnO \cdot Al_2O_3)_{amorphous} + 8KNO_{3(aq)} + 4H_2O_{(l)} \quad (2)$$

$$(ZnO \cdot Al_2O_3)_{amorphous} \xrightarrow{\Delta} ZnAl_2O_{4(s)} \quad (3)$$

On the other hand, when $Ce(NO_3)_3$•$6H_2O$ was added to the precursor solution, Ce^{3+} ions could not form a substitutional solid solution as $ZnAl_{2-x}Ce_xO_4$. They were unable to do so because the ionic radius of the Ce^{3+} ion (101 pm) is significantly larger than that of the Al^{3+} ion (53 pm). Consequently, the Ce^{3+} ions could not replace the Al^{3+} ions at Al sites in the $ZnAl_2O_4$ spinel structure. According to the Hume-Rothery rule[9], an extensive substitutional solid solution occurs only if the relative difference between the ionic radius of Al^{3+} and Ce^{3+} is less than 15%. If the difference in ionic radius is more than 15%, a limited substitutional solid solution occurs. In this study, the difference was about 90%. Therefore, the replacement of Al^{3+} ions with Ce^{3+} ions could not occur. However, the Ce^{3+} ions could react with hydroxide ions to form CeO_2 according to reactions (4−6)[48,49]:

$$Ce(NO_3)_3 \cdot 6H_2O_{(s)} + H_2O_{(l)} \rightarrow Ce^{3+}_{(aq)} + 3NO_3^-{}_{(aq)} \quad (4)$$

$$Ce^{3+}_{(aq)} + 3OH^-_{(aq)} \rightarrow Ce(OH)_{3(s)} \quad (5)$$

$$Ce(OH)_{3(s)} \xrightarrow{\Delta} CeO_{2(s)} + H_2O_{(g)} + 0.5H_{2(g)} \quad (6)$$

Simultaneously, ZnO could be generated according to reactions (7-10)[50]:

$$Zn(NO_3)_2 \cdot 4H_2O_{(s)} + H_2O_{(l)} \rightarrow Zn^{2+}_{(aq)} + 2NO_3^-{}_{(aq)} \quad (7)$$

$$Zn^{2+}_{(aq)} + 4OH^-_{(aq)} \leftrightarrow \left[Zn(OH)_4\right]^{2-}_{(aq)} \quad (8)$$

$$\left[Zn(OH)_4\right]^{2-}_{(aq)} \leftrightarrow Zn(OH)_{2(s)} + 2OH^-_{(aq)} \quad (9)$$

$$Zn(OH)_{2(s)} \xrightarrow{\Delta} ZnO_{(s)} + H_2O_{(g)} \quad (10)$$

Therefore, the products formed as CeO_2/ZnO/$ZnAl_2O_4$ ternary nanocomposites when they were calcined at 800°C in air for 1 h. In this study, it was observed that the intensity of the principal peaks of CeO_2 and ZnO increased as a function of $Ce(NO_3)_3$•$6H_2O$ concentration. Therefore, it could be summarized that amounts of CeO_2 and ZnO formed increasingly.

In this study, chemical composition was determined by XRF technique. When the content of $Ce(NO_3)_3$•$6H_2O$ in the reactions was 0.2, 0.4, 0.6, 0.8 and 1.0 mmol, the CeO_2 content of the products was about 0.92, 2.15, 3.52, 4.30 and 6.06%, respectively, and the ZnO contents were 11.68, 14.41, 16.81, 17.97 and 18.90%. The amount of CeO_2 and ZnO in the product increased as a function of $Ce(NO_3)_3$•$6H_2O$ concentration. This was in good agreement with XRD results.

3.3 Morphological study

As presented in Figure 3, the morphology of pure $ZnAl_2O_4$ spinel nanoparticles was an irregular sponge-like structure made up of agglomerated spherical nanoparticles[7,39,51] but ZnO particles formed a facet structure in a strongly alkaline solution at pH = 11[50]. In this study, ZnO particles formed as rod structures along the *c*-axis, which had the growth velocity in the following order: $v_{(0001)} > v_{(\bar{1}010)} > v_{(\bar{1}011)} > v_{(000\bar{1})}$. At the same time, fluffy particles of CeO_2 formed on the surfaces of $ZnAl_2O_4$ spinel nanoparticles. In agglomerations, many small particles are attracted to one another through chemical bonds and physical forces at interfaces. However, some crystals form a faceted structure due to the different surface energies present at different crystal facets. If particles agglomerated to form a large cluster or a faceted structure, overall surface energy decreased[52] and a more stable system resulted.

3.4 Optical properties

Figure 4 shows the UV-vis diffuse reflectance spectra of $ZnAl_2O_4$ spinel nanoparticles and CeO_2/ZnO/$ZnAl_2O_4$ nanocomposites. The absorption edge of CeO_2/ZnO/$ZnAl_2O_4$ ternary nanocomposites shifted towards longer wavelengths or lower energies compared to the absorption edge of pure $ZnAl_2O_4$ spinel nanoparticles. This shift towards longer wavelengths occurred as a function of the Ce^{3+} ion concentration in the precursor solution and absorption edges shifted to longer wavelengths as the optical band gaps of samples narrowed. Therefore, electrons in valence bands were excited to conduction bands by consuming less photon energy[2].

The optical band gap of samples was evaluated from Tauc plots via Equation 11[2]:

$$(\alpha h\upsilon)^2 = A(h\upsilon - E_g) \quad (11)$$

where α is an absorption coefficient, hυ is the photon energy (h is the Planck's constant and υ is the photon frequency) and E_g is the optical band gap. The plots of $(\alpha h\upsilon)^2$ versus hυ for all samples are presented in Figure 5. To obtain the optical band gap, the linear region was extrapolated to $(\alpha h\upsilon)^2 = 0$. The values of the obtained optical band gaps are given in Table 2.

The optical band gap of $ZnAl_2O_4$ spinel nanoparticles obtained from this experiment was narrower than the optical band gap of bulk $ZnAl_2O_4$ spinel (3.8 eV)[53]. This may have been due to the formation of a subband between valence and conduction bands caused by the formation of localized energy states of defects such as oxygen vacancies, which

Table 2. Principal characterization data of $ZnAl_2O_4$ spinel nanoparticles and $CeO_2/ZnO/ZnAl_2O_4$ nanocomposites.

$Ce(NO_3)_3•6H_2O$ (mmol)	Phase	Shape	E_g (eV)	E_u (eV)	SA (m^2/g)
0	$ZnAl_2O_4$	Irregularly agglomerated sphere	3.220	0.120	37.78
0.2	$CeO_2/ZnO/ZnAl_2O_4$	Rod + Irregularly agglomerated sphere	3.192	0.282	27.98
0.4	$CeO_2/ZnO/ZnAl_2O_4$	Rod + Irregularly agglomerated sphere	3.184	0.284	40.64
0.6	$CeO_2/ZnO/ZnAl_2O_4$	Rod + Irregularly agglomerated sphere	3.180	0.287	41.45
0.8	$CeO_2/ZnO/ZnAl_2O_4$	Rod + Irregularly agglomerated sphere	3.178	0.294	39.45
1.0	$CeO_2/ZnO/ZnAl_2O_4$	Rod + Irregularly agglomerated sphere	3.170	0.299	37.06

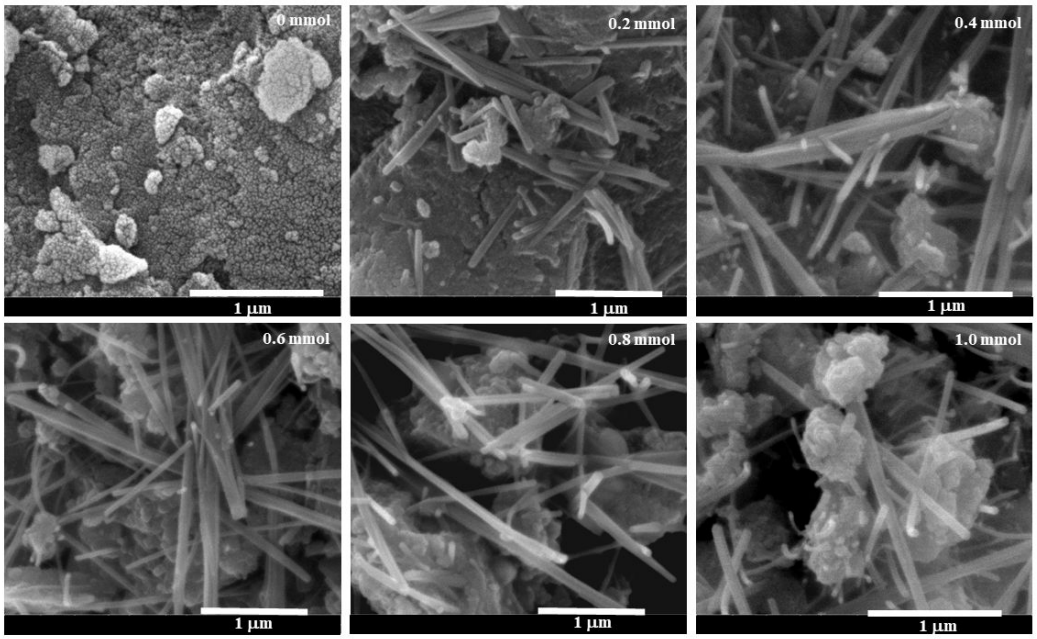

Figure 3. SEM images of $CeO_2/ZnO/ZnAl_2O_4$ nanocomposites prepared at different $Ce(NO_3)_3•6H_2O$ concentrations.

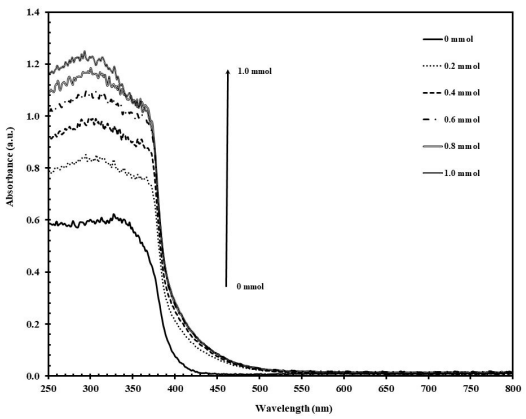

Figure 4. Diffuse reflectance spectra of $CeO_2/ZnO/ZnAl_2O_4$ nanocomposites prepared at different $Ce(NO_3)_3•6H_2O$ concentrations.

resulted in the reduction in optical band gap of $ZnAl_2O_4$ spinel nanoparticles in a previous work[50].

As Ce^{3+} ions were introduced into the precursor solution, secondary phases of CeO_2 and ZnO formed. The value of the optical band gap slightly decreased as a function of the concentration of Ce^{3+} ions in the precursor solution. The reduction in the optical band gap could be attributed to increments in the secondary phases. Khan et al.[10] studied the optical properties of CeO_2 and they found that reductions in the optical band gap were due to the presence of Ce^{3+} ions at grain boundaries, which generated localized energy states from oxygen vacancies within the forbidden band. Consequently, electrons in valence bands could be excited to localized energy states with lower photon energy. In addition, Suwanboon et al.[11] found that the optical band gap of ZnO nanoparticles decreased due to the presence of defects in the ZnO nanoparticles. Band tail energy was created within the forbidden band of ZnO and this event resulted in a reduction in the optical band gap of ZnO nanoparticles. Reports by other research groups[12,54,55] indicated that the optical band gap of CeO_2/ZnO nanocomposites decreased when the mole ratio of Ce to Zn was increased. The reductions were attributed to an increase in the concentration of oxygen vacancies.

In this study, the products formed as $CeO_2/ZnO/ZnAl_2O_4$ ternary nanocomposites and the augmentation in CeO_2 and ZnO secondary phases was in good agreement with the XRD results (Figure 2). The increases in CeO_2 and ZnO contents generated more oxygen vacancies in the ternary nanocomposite systems

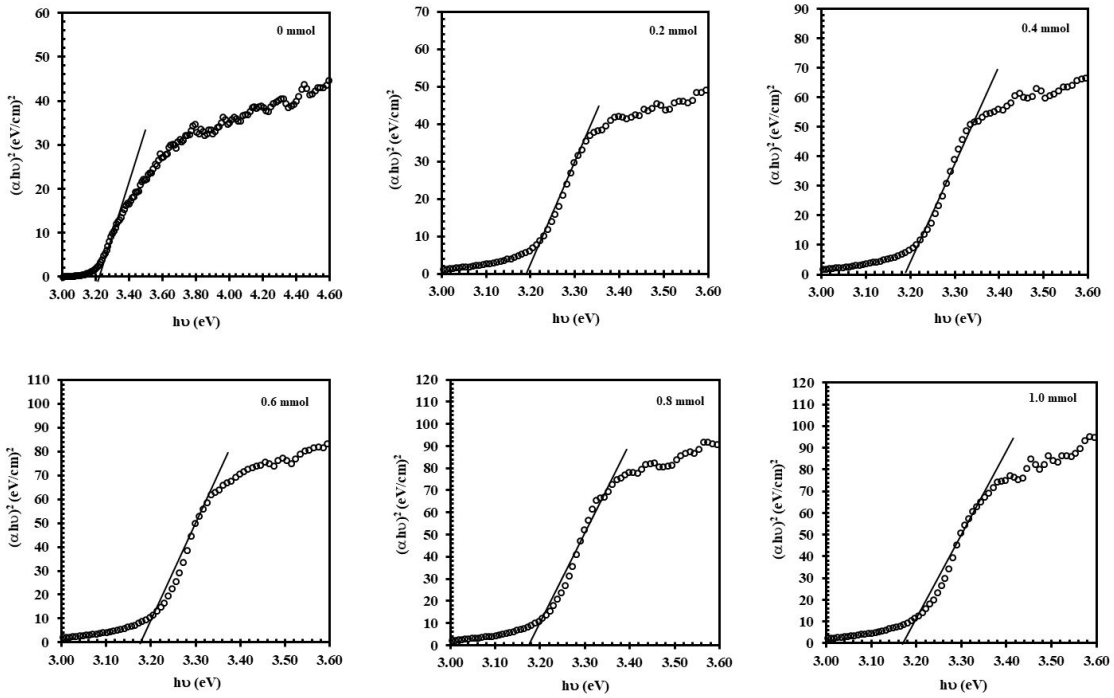

Figure 5. Plots of $(\alpha h\upsilon)^2$ versus $h\upsilon$ of $CeO_2/ZnO/ZnAl_2O_4$ nanocomposites prepared at different $Ce(NO_3)_3 \cdot 6H_2O$ concentrations.

and as a result the optical band gap reduced. To confirm the presence of oxygen vacancies in the samples, the Urbatch energy or band tail energy (E_u) was taken into account. The Urbatch energy was expressed as Equation 12[2]:

$$\alpha = \alpha_0 \left(\frac{E}{E_u} \right) \tag{12}$$

where α is the absorption constant, α_0 is the constant, E is the photon energy and E_u is the Urbatch energy. Urbatch energy was determined from the reciprocal of the slope in the linear region of the plot of $\ln(\alpha)$ versus E (Figure 6). The values of obtained Urbatch energy were presented in Table 2. Urbatch energy was greater when the amount of $Ce(NO_3)_3 \cdot 6H_2O$ in the solution was greater. This behavior was attributed to increments of oxygen vacancy due to increased $Ce(NO_3)_3 \cdot 6H_2O$ concentration and the resultant reductions in optical band gap value.

3.5 Photocatalytic activity

In this study, an aqueous MB solution was used as a dye model. The degradation of MB molecules over $ZnAl_2O_4$ spinel nanoparticles and $CeO_2/ZnO/ZnAl_2O_4$ ternary nanocomposites was observed under UV irradiation.

The strongest intensity of the absorbance peak of the aqueous MB solution centered at a wavelength of 664 nm decreased as a function of irradiation time (Figure 7) as MB contents in the solution were reduced by the photocatalytic reaction. In this study, the MB molecules completely degraded over $CeO_2/ZnO/ZnAl_2O_4$ ternary nanocomposites prepared with 0.2 mmol $Ce(NO_3)_3 \cdot 6H_2O$ within 180 min, whereas they degraded by about 70% over pure $ZnAl_2O_4$ spinel nanoparticles at the same irradiation time.

The degradation of aqueous MB solution over all photocatalysts was determined using Equation 13[2]:

$$\%\text{degradation} = \frac{C_0 - C_t}{C_0} \times 100 = \frac{A_0 - A_t}{A_0} \times 100 \tag{13}$$

where A_0 is the initial absorbance of aqueous MB solution, A_t is the absorbance of aqueous MB solution at time interval t, C_0 is the initial concentration of aqueous MB solution and C_t is the concentration of aqueous MB solution at time interval t.

The degradation of aqueous MB solution was higher over $CeO_2/ZnO/ZnAl_2O_4$ ternary nanocomposites than over $ZnAl_2O_4$ spinel nanoparticles (Figure 8). After exposure to UV radiation for 1 h, MB molecules were completely degraded over the $CeO_2/ZnO/ZnAl_2O_4$ ternary nanocomposites prepared with 1.0 mmol $Ce(NO_3)_3 \cdot 6H_2O$, whereas only about 54% of MB molecules were degraded over pure $ZnAl_2O_4$ spinel nanoparticles. When irradiation time was increased to 2 h, the MB molecules were completely degraded over the $CeO_2/ZnO/ZnAl_2O_4$ ternary nanocomposites prepared with 0.6, 0.8 and 1.0 mmol $Ce(NO_3)_3 \cdot 6H_2O$. At the same irradiation time, the degree of degradation over pure $ZnAl_2O_4$ spinel nanoparticles increased from 54% after 1 h to 64%. After irradiation for 3 h, the MB molecules were completely degraded over all the $CeO_2/ZnO/ZnAl_2O_4$ ternary nanocomposites, whereas only 73% of the MB molecules were degraded over pure $ZnAl_2O_4$ spinel nanoparticles. Besides irradiation time, photocatalytic activity is influenced by various other parameters, including the optical band gap, defects concentration and specific surface area.

The photocatalysts with narrower optical band gaps exhibited higher photocatalytic activity. Since electrons in

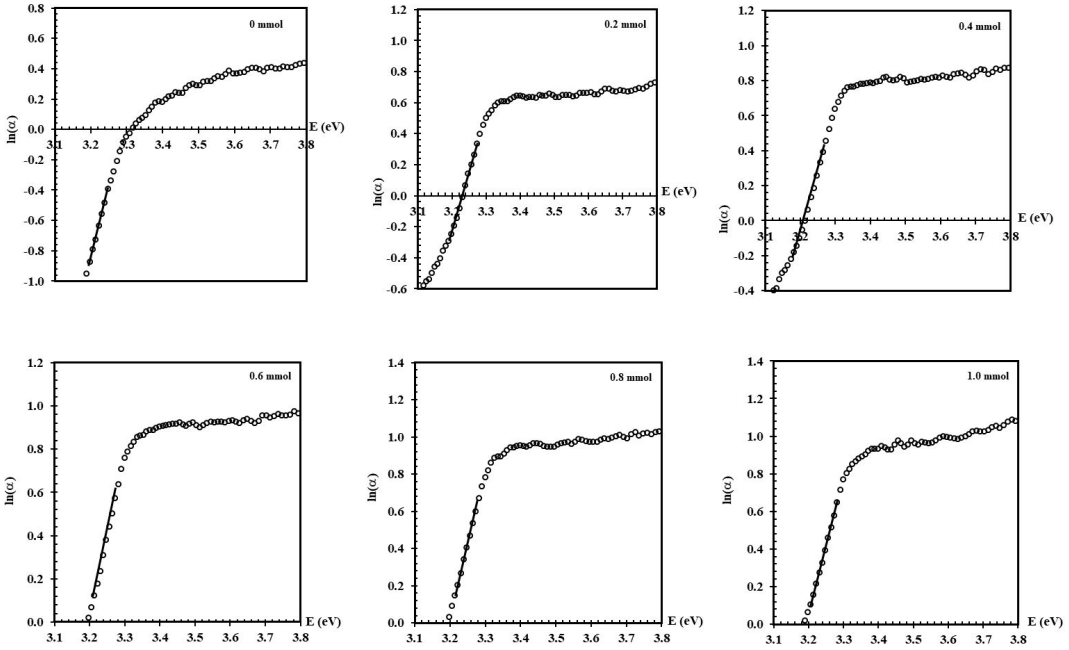

Figure 6. Plots of ln(α) versus E of $CeO_2/ZnO/ZnAl_2O_4$ nanocomposites prepared at different $Ce(NO_3)_3 \cdot 6H_2O$ concentrations.

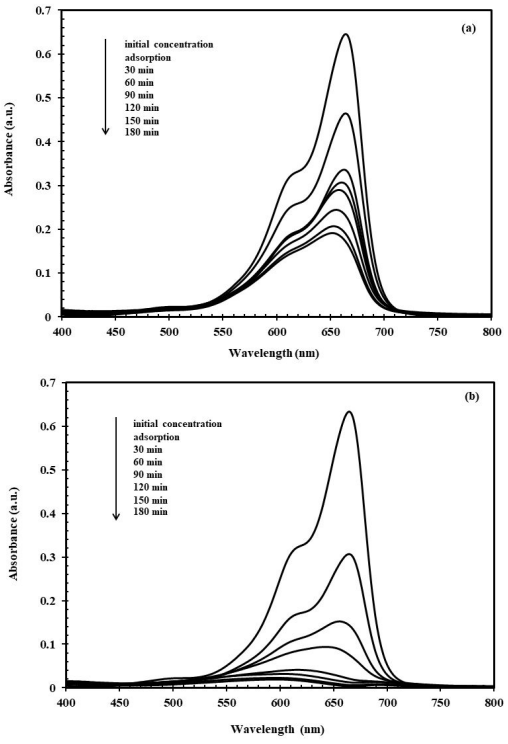

Figure 7. Temporal change in absorbance of (a) $ZnAl_2O_4$ spinel nanoparticles and (b) $CeO_2/ZnO/ZnAl_2O_4$ nanocomposites prepared by 0.2 mmol $Ce(NO_3)_3 \cdot 6H_2O$.

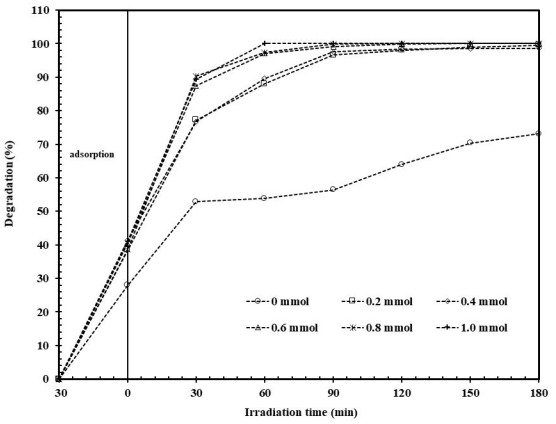

Figure 8. Percentage MB degradation over $CeO_2/ZnO/ZnAl_2O_4$ nanocomposites prepared at different $Ce(NO_3)_3 \cdot 6H_2O$ concentrations.

valence bands could be easily excited to conduction bands, holes (h^+) were left in the valence bands. Photoexcited electrons then reacted with adsorbed O_2 and holes reacted with H_2O at the surface of the photocatalysts to generate superoxide ($\cdot O_2^-$) radicals and hydroxyl ($\cdot OH$) radicals, respectively. These reactive species ($\cdot O_2^-$, $\cdot OH$, h^+) were mostly responsible for the degradation of the MB in solution. The $CeO_2/ZnO/ZnAl_2O_4$ ternary nanocomposites with higher Ce^{3+} concentrations could also adsorb more UV radiation (Figure 4). This result was in good agreement with the higher degradation of aqueous MB solution.

Although the $CeO_2/ZnO/ZnAl_2O_4$ ternary nanocomposites exhibited narrower band gaps than $ZnAl_2O_4$ spinel nanoparticles, the recombination rate of photoexcited electron-hole pairs was retarded because the heterostructure of the $CeO_2/ZnO/ZnAl_2O_4$ ternary nanocomposite could promote the transfer of photoexcited electrons via the interfaces

of the heterostructure, as occurred in the heterostructure of ZnO/NiO/$ZnAl_2O_4$[13]. This transfer of photoexcited electrons contributed to the superior photocatalytic activity of CeO_2/ZnO/$ZnAl_2O_4$ ternary nanocomposites compared to pure $ZnAl_2O_4$ spinel nanoparticles.

Oxygen vacancy is another important parameter that can enhance photocatalytic activity for dye degradation. During the photocatalytic process, oxygen vacancies accept electrons and recombination rates of photoexcited electron-hole pairs are reduced[14]. Moreover, oxygen vacancies can interact with adsorbed O_2 at the surface of photocatalysts, trapping photoexcited electrons to generate $^{\bullet}O_2^-$ radicals. As a result, the degradation of aqueous MB solution improved as a function of the concentration of oxygen vacancies[2].

Photocatalytic activity was also affected by particle shape[2]. ZnO particles with a rod-like structure could enhance photocatalytic activity. The degradation of the aqueous MB solution was improved as a function of {0001} surfaces in which the {0001} facets are strongly reactive in the degradation of MB molecules[15]. ZnO rod structures consist of a positively charged Zn-(0001) terminate and a negatively charged O-$(000\bar{1})$ terminate that created an internal electric field between the positive and negative planes by spontaneous polarization[15]. Therefore, under the influence of this internal electric field, photoexcited electrons transferred to the positive (0001) plane and holes transferred to the negative $(000\bar{1})$ plane. This phenomenon can improve the reduction reaction at the positive (0001) plane and the oxidation reaction at the negative $(000\bar{1})$ plane, so the formation of ZnO in a rod structure can promote the degradation of aqueous MB solution.

The specific surface area of a photocatalyst plays a crucial role in the photocatalytic process. A higher specific surface area provided more active sites; therefore, the photocatalytic reactions involved were accelerated[16]. Considering the specific surface areas listed in Table 2, the specific surface area of the CeO_2/ZnO/$ZnAl_2O_4$ ternary nanocomposite prepared at 0.2 mmol $Ce(NO_3)_3{\cdot}6H_2O$ was smaller than that of the pure $ZnAl_2O_4$ spinel nanoparticle and the specific surface area of the ternary nanocomposite prepared at 1.0 mmol $Ce(NO_3)_3{\bullet}6H_2O$ was equal to the specific surface area of the pure $ZnAl_2O_4$ spinel nanoparticle. However, the photocatalytic activity of both those CeO_2/ZnO/$ZnAl_2O_4$ ternary nanocomposites was greater than the photocatalytic activity of pure $ZnAl_2O_4$ spinel nanoparticles. Therefore, the specific surface areas of the CeO_2/ZnO/$ZnAl_2O_4$ ternary nanocomposites did not significantly influence their photocatalytic activity in this study.

The positions of the valence band potential (E_{VB}) and conduction band potential (E_{CB}) were calculated from Equations 14 and 15[56]:

$$E_{VB} = X - E^e + 0.5E_g \quad (14)$$

$$E_{CB} = E_{VB} - E_g \quad (15)$$

where X is the geometric mean of the Mulliken's electronegativity of CeO_2, ZnO, $ZnAl_2O_4$, E^e is the energy of free electrons on the hydrogen scale (4.50 eV for a normal hydrogen electrode (NHE)) and E_g is the optical band gap energy of CeO_2, ZnO, $ZnAl_2O_4$. The X, E^e, E_g, E_{VB} and E_{CB} values of CeO_2, ZnO, $ZnAl_2O_4$ are listed in Table 3 and a schematic diagram of the electron-hole separation and transport mechanism is presented in Figure 9. To conclude, the possible mechanism of photocatalytic MB degradation over this system irradiated with UV radiation (λ = 315-400 nm) can be proposed as Equations 16-24[57].

Table 3. X, E_g, E_{VB} and E_{CB} of CeO_2, ZnO and $ZnAl_2O_4$.

Constituents	X	E_g (eV)	E_{VB} (eV)	E_{CB} (eV)
CeO_2	5.57[56]	2.88	0.370	-2.510
ZnO	5.79[56]	3.22	0.310	-2.890
$ZnAl_2O_4$	5.49[58]	3.20	0.620	-2.600

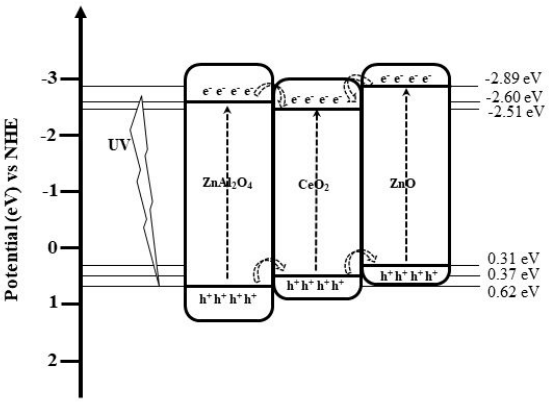

Figure 9. Schematic diagram of electron-hole separation and transport mechanism under UV irradiation of CeO_2/ZnO/$ZnAl_2O_4$ nanocomposite photocatalyst.

$$CeO_2 / ZnO / ZnAl_2O_4 + h\upsilon \rightarrow CeO_2 / ZnO / ZnAl_2O_4(e^-) + CeO_2 / ZnO / ZnAl_2O_4(h^+) \quad (16)$$

$$O_2 + e^- \rightarrow {}^{\bullet}O_2^- \quad (17)$$

$${}^{\bullet}O_2^- + H_2O \rightarrow HO_2 + OH^- \quad (18)$$

$${}^{\bullet}HO_2 + H_2O \rightarrow H_2O_2 + {}^{\bullet}OH \quad (19)$$

$$H_2O_2 + e^- \rightarrow OH^- + {}^{\bullet}OH \quad (20)$$

$$h^+ + OH^- \rightarrow {}^{\bullet}OH \quad (21)$$

$$h^+ + H2O \rightarrow {}^{\bullet}OH + H^+ \quad (22)$$

$$MB + {}^{\bullet}OH / {}^{\bullet}O_2^- \rightarrow \text{degradation product} \quad (23)$$

$$MB + h^+ \rightarrow \text{degradation product} \quad (24)$$

4. Conclusion

CeO_2/ZnO/$ZnAl_2O_4$ ternary nanocomposites were successfully synthesized by a facile co-precipitation method in which the addition of Ce^{3+} ions to the precursor solution disturbed the reaction equilibrium of spinel formation.

SEM revealed the different particle shapes of CeO_2 (fluffy particles), ZnO (rod-like) and $ZnAl_2O_4$ (irregular sponge-like). The optical band gap of CeO_2/ZnO/$ZnAl_2O_4$ ternary nanocomposites slightly shifted to a longer wavelength compared with $ZnAl_2O_4$ spinel nanoparticles. The defect concentration of oxygen vacancies increased as a function of Ce^{3+} ion concentration. The photocatalytic activity of the CeO_2/ZnO/$ZnAl_2O_4$ ternary nanocomposites depended significantly on the particle shape of the loading, the optical band gap and the defect concentration.

5. Acknowledgement

This work was supported by the budget revenue of Prince of Songkla University under the contract number SCI6202036S. The authors would like to thank the Center of Excellence for Innovation in Chemistry (PERCH-CIC), Ministry of Higher Education, Science, Research and Innovation, Thailand. The authors would like to acknowledge Mr. Thomas Duncan Coyne for assistance with the English.

6. References

1. Katheresan V, Kansedo J, Lau SY. Efficiency of various recent wastewater dye removal methods: A review. J Environ Chem Eng. 2018;6:4676-97.
2. Suwanboon S, Amornpitoksuk P, Randorn C. Effect of tartaric acid as a structure-directing agent ZnO morphologies and their physical and photocatalytic properties. Ceram Int. 2019;45:2111-6.
3. Gong J, Meng F, Fan Z, Li H, Du Z. Template-free controlled hydrothermal sysnthesis for monodisperse flowerlike porous CeO_2 microspheres and their superior reduction of NO with NH_3. J Alloys Compd. 2017;690:677-87.
4. Akika FZ, Benamira M, Lahmar H, Tibera A, Chabi R, Avramova I, et al. Structural and optical properties of Cu-substitution of $NiAl_2O_4$ and their photocatalytic activity towards Congo red under solar light irradiation. J Photochem Photobiol Chem. 2018;364:542-50.
5. Chaudhary A, Mohammad A, Mobin SM. Facile synthesis of phase pure $ZnAl_2O_4$ nanoparticles for effective photocatalytic degradation of organic dyes. Mater Sci Eng B. 2018;227:136-44.
6. Zhang L, Yan J, Zhou M, Yang Y, Liu YN. Fabrication and photocatalytic properties of spheres-in-spheres ZnO/$ZnAl_2O_4$ composite hollow microspheres. Appl Surf Sci. 2013;268:237-45.
7. Sumathi S, Kavipriya A. Structural, optical and photocatalytic activity of cerium doped zinc aluminate. Solid State Sci. 2017;65:52-60.
8. Suwanboon S, Amornpitoksuk P, Bangrak P, Randorn C. Physical and chemical properties of multifunctional ZnO nanostructures prepared by precipitation and hydrothermal methods. Ceram Int. 2014;40:975-83.
9. Suwanboon S, Amornpitoksuk P, Bangrak P, Muensit N. Optical, photocatalytic and bactericidal properties of $Zn_{1-x}La_xO$ and $Zn_{1-x}Mg_xO$ nanostructures prepared by a sol-gel method. Ceram Int. 2013;39:5597-608.
10. Khan MM, Ansari SA, Pradhan D, Han DH, Lee J, Cho MH. Defect-induced band gap narrowed CeO_2 nanostructures for visible light activities. Ind Eng Chem Res. 2014;53:9754-63.
11. Klubnuan S, Suwanboon S, Amornpitoksuk P. Effects of optical band gap energy, band tail energy and particle shape on photocatalytic activities of different ZnO nanostructures prepared by a hydrothermal method. Opt Mater. 2016;53:134-41.
12. Lv Z, Zhong Q, Ou M. Utilizing peroxide as precursor for the synthesis of CeO_2/ZnO composite oxide with enhanced photocatalytic activity. Appl Surf Sci. 2016;376:91-6.
13. Zhang L, Dai CH, Zhang XX, Liu YN, Yan JH. Synthesis and highly efficient photocatalytic activity of mixed oxides derived from ZnNiAl layered double hydroxides. Trans Nonferrous Met Soc China. 2016;26:2380-9.
14. Balamurugan S, Balu AR, Srivind J, Usharani K, Narasimman V, Suganya M, et al. CdO-Al_2O_3-A composite material with enhanced photocatalytic activity against the degradation of MY dye. Vacuum. 2019;159:9-16.
15. Chen Y, Zhang L, Ning L, Zhang C, Zhao H, Liu B, et al. Superior photocatalytic activity of porous wurtzite ZnO nanosheets with exposed {001} facets and a charge separation model between polar (001) and (00-1) surfaces. Chem Eng J. 2015;264:557-64.
16. Kirankumar VS, Sumathi S. Catalytic activity of bismuth doped zinc aluminate nanoparticles towards environmental remediation. Mater Res Bull. 2017;93:74-82.
17. Saleh TA, Gupta VK. Photo-catalyzed degradation of hazardous dye methyl orange by use of a composite catalyst consisting of multi-walled carbon nanotubes and titanium dioxide. J Colloid Interface Sci. 2012;371:101-6.
18. Saravanan R, Sacari E, Gracia F, Khan MM, Mosquera E, Gupta VK. Conducting PANI stimulated ZnO system for visible light photocatalytic degradation of coloured dyes. J Mol Liq. 2016;211:1029-33.
19. Saravanan R, Karthikeyan S, Gupta VK, Sekaran G, Narayanan V, Stephen A. Enhanced photocatalytic activity of ZnO/CuO nanocomposite for the degradation of textile dye on visible light illumination. Mater Sci Eng C. 2013;33:91-8.
20. Saravanan R, Gupta VK, Prakash T, Narayanan V, Stephen A. Synthesis, characterization and photocatalytic activity of novel Hg doped ZnO nanorods prepared by thermal decomposition method. J Mol Liq. 2013;178:88-93.
21. Saleh TA, Gupta VK. Functionalization of tungsten oxide into MWCNT and its application for sunlight-induced degradation of rhodamine B. J Colloid Interface Sci. 2011;362:337-44.
22. Saravanan R, Khan MM, Gupta VK, Mosquera E, Gracia F, Narayanan V, et al. ZnO/Ag/CdO nanocomposite for visible light-induced photocatalytic degradation of industrial textile effluents. J Colloid Interface Sci. 2015;452:126-33.
23. Saravanan R, Khan MM, Gupta VK, Mosquera E, Gracia F, Narayanan V, et al. ZnO/Ag/Mn_2O_3 nanocomposite for visible light-induced industrial textile effluent degradation, uric acid and ascorbic acid sensing and antimicrobial activity. RSC Advances. 2015;5:34645-51.
24. Zhao X, Yang H, Cui Z, Yi Z, Yu H. Synergistically enhanced photocatalytic performance of $Bi_4Ti_3O_{12}$ nanosheets by Au and Ag nanoparticles. J Mater Sci Mater Electron. 2019;30:13785-96.
25. Yan Y, Yang H, Yi Z, Xian T. $NaBH_4$-reduction induced evolution of Bi nanoparticles from BiOCl nanoplates and construction of promising Bi@BiOCl hybrid photocatalysts. Catalysts. 2019;9:795.
26. Lahmer MA. First-principles study of the structural, electronic, and optical properties of the clean and O-deficient $ZnAl_2O_4$(110) surfaces. Surf Sci. 2018;677:105-14.
27. Shahbazi H, Shokrollahi H, Alhaji A. Optimizing the gel-casting parameters in synthesis of $MgAl_2O_4$ spinel. J Alloys Compd. 2017;712:732-41.
28. Hussain M, Islam MU, Meydan T, Cuenca JA, Melikhov Y, Mustafa G, et al. Microwave absorption properties of CoGd substituted $ZnFe_2O_4$ ferrites synthesized by co-precipitation technique. Ceram Int. 2018;44:5909-14.
29. Talic B, Hendriksen PV, Wiik K, Lein HL. Thermal expansion and electrical conductivity of Fe and Cu doped $MnCo_2O_4$ spinel. Solid State Ion. 2018;326:90-9.
30. Vediappan K, Prasanna K, Shanmugan S, Gnanamuthu RM, Lee CW. Structural stability and electrochemical properties of gadolinium-substituted $LiGd_xMn_{2-x}O_4$ spinel as cathode

materials for Li-ion rechargeable batteries. Appl Surf Sci. 2018;449:412-20.
31. Daffé N, Choueikani F, Neveu S, Arrio MA, Juhin A, Ohresser P, et al. Magnetic anisotropies and cationic distribution in $CoFe_2O_4$ nanoparticles prepared by co-precipitation route: Influence of particle size and stoichiometry. J Magn Magn Mater. 2018;460:243-52.
32. Ravikumar BS, Nagabhushana H, Sharma SC, Nagabhushana BM. Low temperature synthesis, structural and dosimetric characterization of $ZnAl_2O_4:Ce^{3+}$ nanophosphor. Spectrochimica Acta, Part A. 2014;122:489-98.
33. Mindru I, Gingasu D, Patron L, Marinescu G, Calderon-Moreno JM, Diamandescu L, et al. Tb^{3+}-doped alkaline-earth aluminates: Synthesis, characterization and optical properties. Mater Res Bull. 2017;85:240-8.
34. Guan MY, Xu DM, Song YF, Guo Y. $ZnO/ZnAl_2O_4$ prepared by calcination of ZnAl layered double hydroxides for ethanol sensing. Sens Actuators B Chem. 2013;188:1148-54.
35. Okal J, Zawadzki M, Krajczyk L. Light alkane oxidation over Ru supported on $ZnAl_2O_4$, CeO_2 and Al_2O_3. Catal Today. 2011;76:173-6.
36. Motloung SV, Dejene FB, Koao LF, Ntwaeaborwa OM, Swart HC, Motaung TE, et al. Structural and optical studies of $ZnAl_2O_4:x\%Cu^{2+}$ ($0 < x \leq 1.25$) nanophosphors synthesized via citrate sol-gel route. Opt Mater. 2017;64:26-32.
37. He C, Ji H, Huang Z, Zhang X, Liu Y, Fang M, et al. Preparation, structure, luminescence properties of europium doped zinc spinel structure green-emitting phosphor $ZnAl_2O_4:Eu^{2+}$. J Rare Earths. 2018;36:931-8.
38. Motloung SV, Tsega M, Dejene FB, Swart HC, Ntwaeaborwa OM, Koao LF, et al. Effect of annealing temperature on structural and optical properties of $ZnAl_2O_4$:1.5%Pb^{2+} nanocrystals synthesized via sol-gel reaction. J Alloys Compd. 2016;677:72-9.
39. Motloung SV, Tshabalala KG, Kroon RE, Hlatshwayo TT, Mlambo M, Mpelane S. Effect of Tb^{3+} concentration on the structure and optical properties of triply doped $ZnAl_2O_4$:1%Ce^{3+}, 1%Eu^{3+}, x%Tb^{3+} nano-phosphors synthesized via citrate sol-gel method. J Mol Struct. 2019;175:241-52.
40. Ma J, Qi G, Chen Y, Liu S, Cao W, Wang X. Luminescence property of $ZnAl_2O_4:Cr^{3+}$ phosphors co-doped by different cations. Ceram Int. 2018;44:11898-900.
41. Singh V, Singh N, Pathak MS, Dubey V, Singh PK. Annealing effects on the luminescence properties of Ce doped $ZnAl_2O_4$ produced by combustion synthesis. Optik (Stuttg). 2018;155:285-91.
42. Mekprasart W, Boonyarattanakalin K, Pecharapa W, Ishihara KN. Optical characteristics of samarium doped $ZnAl_2O_4$ nanomaterials synthesized by vibrational milling process. Materials Today: Proceedings. 2018;5:14126-30.
43. Dwibedi D, Murugesan C, Leskes M, Barpanda P. Role of annealing temperature on cation ordering in hydrothermally prepared zinc aluminate ($ZnAl_2O_4$) spinel. Mater Res Bull. 2018;98:219-24.
44. Kumari P, Dwivedi Y, Bahadur A. Analysis of bright red-orange emitting $Mn^{2+}:ZnAl_2O_4$ spinel nanophosphor. Optik (Stuttg). 2018;154:126-32.
45. Zawadzki M. Synthesis of nanosized and microporous zinc aluminate spinel by microwave assisted hydrothermal method (microwave-hydrothermal synthesis of $ZnAl_2O_4$). Solid State Sci. 2006;8:14-8.
46. Gimenez P, Fereres S. Effect of heating rates and composition on the thermal decomposition of nitrate based molten salts. Energy Procedia. 2015;69:654-62.
47. Grigorie AC, Muntean C, Vlase G, Ştefănescu M. Synthesis and characterization of $ZnAl_2O_4$ spinel from Zn(II) and Al(III) carboxylates. J Therm Anal Calorim. 2018;131:183-9.
48. Abellan P, Moser TH, Lucas IT, Grate JW, Evans J, Browning ND. The formation of cerium(III) hydroxide nanoparticles by a radiation mediated increase in local pH. RSC Advances. 2017;7:3831-7.
49. Bouchaud B, Balmain J, Bonnet G, Pedraza F. pH-distribution of cerium species in aqueous systems. J Rare Earths. 2012;30:559-62.
50. Jitti-a-porn P, Suwanboon S, Amornpitoksuk P, Patarapaiboolchai O. Defects and the optical band gap of ZnO nanoparticles prepared by a grinding method. J Ceram Process Res. 2011;12:85-9.
51. Anand GT, Kennedy LJ, Aruldoss U, Vijaya JJ. Structural, optical and magnetic properties of $Zn_{1-x}Mn_xAl_2O_4$ ($0 \leq x \leq 0.5$) spinel nanostructures by one-pot microwave combustion. J Mol Struct. 2015;1084:244-53.
52. Cao G. *Nanostructures and nanomaterials: Synthesis, properties and application*. London: Imperial College Press; 2004.
53. Anand GT, Kennedy LJ, Vijaya JJ. Microwave combustion synthesis, structural, optical and magnetic properties of $Zn_{1-x}Co_xAl_2O_4$ ($0 \leq x \leq 0.5$) spinel nanostructures. J Alloys Compd. 2013;581:558-66.
54. Suwanboon S, Amornpitoksuk P, Bangrak P. The improvement of the band gap energy and antibacterial activities of CeO_2/ZnO nanocomposites prepared by high energy ball milling. Warasan Khana Witthayasat Maha Witthayalai Chiang Mai. 2018;45:1129-37.
55. He G, Fan H, Wang Z. Enhanced optical properties of heterostructured ZnO/CeO_2 nanocomposite fabricated by one-pot hydrothermal method: fluorescence and ultraviolet absorption and visible light transparency. Opt Mater. 2018;38:145-53.
56. Rajendran S, Khan MM, Gracia F, Qin J, Gupta VK, Arumainathan S. Ce^{3+}-ion-induced visible-light photocatalytic degradation and electrochemical activity of ZnO/CeO_2 nanocomposite. Sci Rep. 2016;6:31641.
57. Liu J, Luo Z, Han W, Zhao Y, Li P. Preparation of ZnO/Bi_2WO_6 heterostructures with improved photocatalytic performance. Mater Sci Semicond Process. 2020;106:104761.
58. Tian Q, Fang G, Ding L, Ran M, Zhang H, Pan A, et al. $ZnAl_2O_4/Bi_2MoO_6$ heterostructures with enhanced photocatalytic activity for the treatment of organic pollutants and eucalyptus chemomechanical pulp wastewater. Mater Chem Phys. 2020;241:122299.